DTU Library

Examining the rudimentary steps of the oxygen reduction reaction on single-atomic Pt using Ti-based non-oxide supports

Tak, Young Joo; Yang, Sungeun; Lee, Hyunjoo; Lim, Dong Hee; Soon, Aloysius

Examining the rudimentary steps of the oxygen reduction reaction on single-atomic Pt using Ti-based non-oxide supports

Young-Joo Tak,[1] Sungeun Yang,[2, 3] Hyunjoo Lee,[2] Dong-Hee Lim,[4, *] and Aloysius Soon[1, *]

[1]*Department of Materials Science and Engineering, Yonsei University, Seoul 03722, Korea*

[2]*Department of Chemical and Biomolecular Engineering,*
Korea Advanced Institute of Science and Technology, Daejeon 34141, Korea

[3]*Department of Physics, Technical University of Denmark, Lyngby, Denmark*

[4]*Department of Environmental Engineering,*
Chungbuk National University, Cheongju 28644, Korea

(Dated: September 1, 2017)

In the attempt to reduce the high-cost and improve the overall durability of Pt-based electrocatalysts for the oxygen reduction reaction (ORR), density-functional theory (DFT) calculations have been performed to study the energetics of the elementary steps that occur during ORR on TiN(100)- and TiC(100)-supported single Pt atoms. The O_2 and OOH^* dissociation processes on Pt/TiN(100) are determined to be non-activated (i.e. "barrierless" dissociation) while an activation energy barrier of 0.19 and 0.51 eV is found for these dissociation processes on Pt/TiC(100), respectively. Moreover, the series pathway (which is characterized by the stable OOH^* molecular intermediate) on Pt/TiC(100) is predicted to be more favorable than the direct pathway. Our electronic structure analysis supports a strong synergistic co-operative effect by these non-oxide supports (TiN and TiC) on the reduced state of the single-atom Pt catalyst, and directly influences the rudimentary ORR steps on these single-atom platinized supports.

I. INTRODUCTION

Amongst many oxygen-related (electro)chemical reactions, oxygen reduction reaction (ORR) [1–3] is one of the fundamentally important and technologically relevant reactions for many clean energy processes, e.g. hydrogen-based fuel cell technology [4]. Due to its generally low operating temperatures and overall light weight, the proton exchange membrane fuel cells (PEM FCs) are often considered as a suitable candidate for portable energy applications, such as hydrogen-fuel operated vehicles [5]. However, the overall efficiency of these PEM FCs are often plagued by the slow kinetics of the ORR, high cost of the platinum catalyst, and long-term durability issues [5, 6].

---

* Corresponding authors. E-mail: aloysius.soon@yonsei.ac.kr; limkrs@cbnu.ac.kr

Typeset by REVTₑX

To address these limitations, many have attempted to systematically study and rationally design new nanocatalyst systems which could be more efficient and durable for PEM FC applications [7–10].

It has been suggested that one of the more promising approaches is to develop highly-reactive and exceptionally-selective single-atom nanocatalyst systems (SAC) on ultra-durable functional supports [11]. Single-atom nanocatalyst systems are the state-of-art "recipe" which enhances the catalytic reactivity (per atom efficiency) and yet drastically reduce the precious metal loading at the same time. Of late, it has been shown that this breakthrough of marrying both nanotechnology and catalysis science has led to an impressive gain in the overall performance of many catalytic reactions involving precious metal catalysis [11–17].
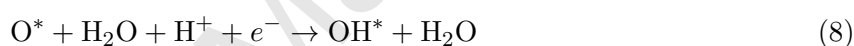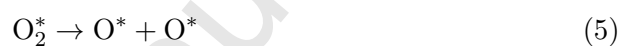
In the effort to improve catalyst durability on the whole, classic conductive refractory materials (e.g. TiN and TiC) have been suggested as non-conventional support candidates for Pt-based single-atom nanocatalysts. TiN and TiC are well-known for their high resistance to weathering and corrosion, and excellent electrical conductivity [18–22], er electrochemical reactions via strong support-catalyst interactions [23–26]. and from recent studies, it has also been shown that TiN-supported Pt nanocatalysts may provide a means to mitigate the long-standing problem of CO poisoning of the Pt catalyst [27, 28], as well as to boost the reactivity of the ORR and other electrochemical reactions via strong support-catalyst interactions [23–25]. The other drawback of Pt catalyst that may hinder the reactivity of ORR is the commonly reported O^* and OH^* poisoning [29]. This is often thought to be associated with the high adsorption energy of O^* and OH^* which inhibits the effective adsorption of O_2. Given that both O^* and OH^* are important reaction intermediates in the ORR, the adsorption behavior and the associated energetics of these intermediates will also be discussed in this work. Although much less is known about the reactions on TiC as a non-conventional support for the Pt catalyst [30, 31], given its similar crystal structure and physio-chemical properties to TiN [32, 33], it will be interesting to study and compare the role of these non-conventional supports for the single-atom Pt nanocatalysts in the ORR.

$$O_2 + 4\,H^+ + 4\,e^- \rightarrow 2\,H_2O \tag{1}$$

$$O_2 + 2\,H^+ + 2\,e^- \rightarrow H_2O_2 \tag{2}$$

$$H_2O_2 + 2\,H^+ + 2\,e^- \rightarrow 2\,H_2O \tag{3}$$

To date, the ORR is commonly known to proceed via either the so-called "Direct (4-electron)" (Equation 1) or "Series (2-electron)" (Equations 2 and 3) mechanistic reaction pathways [29, 34–

36]. Initially, it was first proposed that the ORR assumes the direct (4-electron) pathway on Pt single crystal surfaces [37]. Markovic and co-workers then suggested that the series (2-electron) pathway may be more favorable on Pt and Pt alloy nanocatalysts [38]. Adding to the controversy, others have found that a complex "parallel" pathway which includes both the direct (4-electron) and series (2-electron) steps may yet be another possibility [39, 40]. Hitherto, the specific ORR pathway on Pt nanocatalysts is still very much debated, and is indeed very much sensitive to the actual technical conditions under which the ORR is conducted, as well as the preparation method of the catalyst used.

Here, we briefly present the rudimentary reaction steps in the ORR. Via the 4-electron pathway, the proposed elementary steps are [35]:

$$O_2 \rightarrow O_2^* \tag{4}$$

$$O_2^* \rightarrow O^* + O^* \tag{5}$$

$$O^* + O^* + H^+ + e^- \rightarrow O^* + OH^* \tag{6}$$

$$O^* + OH^* + H^+ + e^- \rightarrow O^* + H_2O \tag{7}$$

$$O^* + H_2O + H^+ + e^- \rightarrow OH^* + H_2O \tag{8}$$

$$OH^* + H_2O + H^+ + e^- \rightarrow 2\,H_2O \tag{9}$$

where O_2 is directly reduced to H_2O molecules via dissociated O and OH molecular fragments on the catalyst surface. Here, the adsorbed species are superscripted with the *.

To afford a direct comparison between the elementary steps in both the 4- and 2-electron pathway, we are simply replacing Equations 5 and 6 by the following Equations 10 and 11, respectively [35]:

$$O_2^* + H^+ + e^- \rightarrow OOH^* \tag{10}$$

$$OOH^* \rightarrow O^* + OH^* \tag{11}$$

where the surface-bound O_2^* associatively forms the OOH^* bypassing the actual production of H_2O_2.

In passing, we have recently examined and reported the actual mechanistic pathway of H_2O_2 formation on Pt/TiN and Pt/TiC catalysis system using both theory and experiments [25]. There, we demonstrate that a change in the support from TiN to TiC dramatically influenced the overall catalytic activity, selectivity and stability. As compared to the TiN-supported SAC, TiC-supported

SAC shows a much superior reactivity and selectivity towards H_2O_2 formation (rather than the generation of H_2O). Using density-functional theory (DFT) transition-state calculations, we have indeed elucidated the reaction mechanism for this preference. Through that work, we have affirmed the importance of the support chemistry as much as the active metal atoms which have enjoyed more spotlight.

For a more in-depth atomistic picture of our previous findings, in this work, we extend our study of the rudimentary reaction steps of the ORR via first-principles DFT calculations for both the Pt/TiN and Pt/TiC systems. Although our previous work focused on their excellent selectivity towards H_2O_2 formation (which maybe seen as an *side product* of the ORR), we would like to emphasize that in this work our attention is centred on addressing the full ORR pathway including the desired formation of H_2O (i.e. the final key reaction step of the ORR). Given that the actual mechanistic pathway can be very much sensitive to the immediate chemical environment and the local surface geometry and chemistry of the catalyst systems, the role of these non-conventional TiN and TiC supports on the single-atom Pt nancatalysts for the ORR via both the direct (4-electron) and series (2-electron) pathways will be carefully examined and compared via first-principles DFT calculations coupled with the computational hydrogen electrode (CHE) model [29].

II. METHODS AND MODELS

Spin-polarized DFT calculations in this work are performed using the generalized gradient approximation (GGA) to the exchange-correlation functional due to Perdew, Burke and Ernzerhof (PBE) [41] and the projector augmented-wave (PAW) method as implemented in the Vienna *Ab initio* Simulations Package (VASP) [42–44]. A planewave kinetic energy cutoff of $500\,\mathrm{eV}$ and a vacuum region of $18\,\text{Å}$ between repeating periodic images are used for the calculations of all surface slab models. A Monkhorst-Pack $4\times4\times1$ **k**-point mesh is used for the $p(3\times3)$ TiN(100) and TiC(100) supercells.

For single-atom Pt/TiN system, we adopt the TiN(100) surface with a Pt atom embedded at the surface N vacancy site as identified as the most relevant catalyst model in our previous works (thereafter referred to as "Pt/TiN(100)") [27, 45]. For the TiC support, ensuing Ref 45, we have also identified TiC(100) with a surface C vacancy as the relevant surface model for Pt adsorption studies and conclude that the single Pt atom binds most favourably at the surface C vacancy site on TiC(100) under C-lean conditions (thereafter referred to as "Pt/TiC(100)"). Details of these calculations can be found in the Supplemental Material (Figures S1 to S4) [46].

Specifically, these slab models are then used for atomic/molecular (e.g. O, H, OH, and OOH) adsorption studies where these species are adsorbed on 4 atomic layers of Pt/TiN(100) and Pt/TiC(100), respectively, ensuring a lateral distance of $\sim 9\,\text{Å}$ between the molecular fragments and their periodic images. Here, we fully relax the atomic coordinates for all structures, while keeping the bottom two layers of the TiN(100) and TiC(100) substrate fixed to its bulk positions. Since asymmetrical surface slabs are used, a dipole correction has been employed for all slab calculations.

In this work, all DFT calculations have been tested for convergence with respect to kinetic energy cutoff, $\mathbf{k}$-point grid, vacuum separation between repeated slabs, and slab thickness, where total energies and forces do not change more than $20\,\text{meV}$ and $0.02\,\text{eV/Å}^{-1}$, respectively.

To assess the thermodynamic stability of various molecular fragments and intermediates on both Pt/TiN(100) and Pt/TiC(100), we calculate the adsorption energy, E_{ad} for each adsorbate by

$$E_{\text{ad}} = E_{\text{tot}} - E_{\text{TiX}}^{\text{Pt}} - E_{\text{M}} + \Delta\text{ZPE} \quad , \tag{12}$$

where E_{tot} and $E_{\text{TiX}}^{\text{Pt}}$ are the total energies of the optimized adsorbate/catalyst system and the specific Pt/TiX(100) support (where Pt/TiX is either Pt/TiN or Pt/TiC), respectively. E_{M} refers to the total energy of gas-phase species considered in this work, while the last term ΔZPE is the change in the zero point energy of these gas-phase species upon adsorption. The vibrational frequencies of the gas-phase species are estimated determined within the harmonic approximation model (with the "frozen slab" approach where the contributions of the slab atoms to the vibrational free energy are not considered) [47]. Here, all molecular species are taken as charge neutral [29].

Aligning with previous theoretical studies on electrochemical reactions, the computational hydrogen electrode (CHE) model due to Nørskov et $al.$ [29] is also employed in this work to evaluate the electrochemical reaction pathways via free energy calculations of the ORR intermediates. The change in the free energy (ΔG) is calculated using

$$\Delta G = \Delta E + \Delta\text{ZPE} - T\Delta S \quad , \tag{13}$$

where ΔE, ΔZPE and ΔS are the respective changes in the total DFT energy, the zero-point energy, and the entropy. For convenience, the entropy values of the molecular species are obtained from the literature [34]. Here, the temperature (T) is taken as $298.15\,\text{K}$ (i.e. under ambient

conditions). Further calculation details can be found in the Supplemental Material.

Under the consideration of an electropotential bias, we have also applied a numerical shift of $-eU$ to the ΔG value where e is the elementary positive charge and U is the applied electropotential bias. For this work, we have adopted the standard electrode potential reaction of $H_2 + 1/2$ $O_2 \rightarrow H_2O$, and used a U value of $1.23\,\mathrm{V}$ for the theoretical description of the ORR. Here, the enthalpic temperature correction ($\int C_p\,dT$) for the adsorbate/substrate system has been neglected due to its fairly small contribution to the total free energy (approximately $0.005 \sim 0.10\,\mathrm{eV}$) but has been included for gas-phase molecule calculations [47]. Zero-point energy corrections and entropic contributions [29, 48] are explicitly included in our free energy calculations for all gas-phase molecules.

For the O_2 and OOH dissociation step (cf. Equations 5 and 11), the activation energy barrier for these two adsorbed species is calculated using the climbing image nudged elastic band (CI-NEB) method, as is commonly used to locate the minimum energy paths (MEPs) and the corresponding transition states of adsorbate molecules on the transition metal surface [49]. For the elementary steps that involve co-adsorbed species (e.g. in Equations 6 and 11), following Ref. 50, we mitigate the lateral intermolecular interactions by first calculating each adsorbed species individually in separate $p(3 \times 3)$ surface supercells and then summing up their energetics.

The electronic structure of these platinized supports and their adsorbates are then investigated by calculating the electronic charges and their changes/fluctuations for each step of the ORR. Here we adopt the Bader charge analysis scheme [51, 52] as implemented by Henkelman et al. [53] Specifically, the Bader charges are calculated for the optimized structures of bulk Pt, bulk TiN, bulk TiC, and the various gas-phase molecular species considered in this work. We then proceed to determine the Bader charges for the Pt/TiN(100) and Pt/TiC(100) – with and without adsorbates – to compute the excess Bader charges (Δq) with respect to the bulk/molecular systems. The Δq will then allow one to trace the amount of charge redistribution in the platinized system for each step of the ORR.

III. RESULTS AND DISCUSSION

A. Molecular adsorption of ORR intermediates on platinized supports

Before considering the ORR pathways on Pt/TiN(100) and Pt/TiC(100), we will first discuss the relative stability of the ORR intermediate molecular species (i.e. O, O_2, OH, and OOH) on
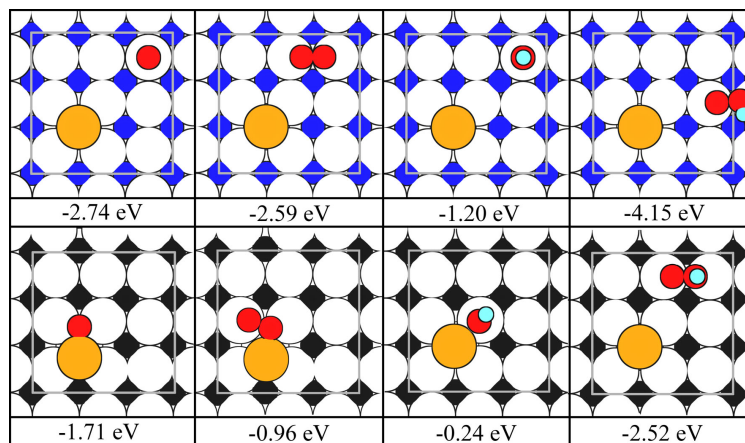
FIG. 1. (Color online) Calculated adsorption energy E_{ad}, for each adsorbate (cf. Equation 12) at the top views of most stable adsorption sites. From left to right, O, O_2, OH and OOH on Pt/TiN(100) (upper panel) and Pt/TiC(100) (lower panel) are shown. The N, C, Ti, Pt, O and H atoms are depicted by blue, black, white, orange, red and cyan colored circles, respectively.

Pt/TiN(100) and Pt/TiC(100), respectively. As seen in the upper panel of Figure 1, we have considered various adsorption sites in a $p(3 \times 3)$ surface supercell and show only the most stable adsorption sites for each molecular species on Pt/TiN(100) (with the calculated adsorption energy per species, E_{ad}, cf. Equation 12, presented below each case). The same is shown for Pt/TiC(100) in the lower panel of Figure 1. Here, a negative value of E_{ad} will indicate a thermodynamically stable adsorption site.

Specifically, for O and OH on Pt/TiN(100), they adsorb preferentially at the Ti top site (furthest away from the Pt atom) with the corresponding E_{ad} of $-2.74 \, \text{eV}$ and $-1.20 \, \text{eV}$, respectively, while O_2 binds selectively at the Ti-Ti bridge site far away from the embeded Pt atom with E_{ad} of $-2.59 \, \text{eV}$, in agreement with an earlier study [54]. In the case of OOH*, the site found to be stable for the molecular adsorption of OOH* was the Ti top site with an adsorption energy of $-4.15 \, \text{eV}$.

In contrast, for Pt/TiC(100), O adsorbs preferentially at the Ti-Ti bridge site closest to the Pt atom ($E_{\text{ad}} = -1.71 \, \text{eV}$), while O_2 preferred the tilted Ti-Ti bridge site with E_{ad} of $-0.96 \, \text{eV}$. OH is most stable at the Ti top site nearest the Pt atom ($E_{\text{ad}} = -0.24 \, \text{eV}$). Interestingly, for all considered binding sites, the molecular adsorption of OOH* is highly favored, with the most thermodynamically stable site being the Ti-Ti bridge site with E_{ad} of $-2.52 \, \text{eV}$.

Notably, we would like to further discuss and compare the adsorption behavior of the OOH* fragment on both Pt/TiN(100) as well as Pt/TiC(100), given that the stability and molecular adsorption of this intermediate is key to distinguishing either the direct (4-electron) or series (2-electron) ORR pathway might be preferred (cf. Equations 5 and 10).

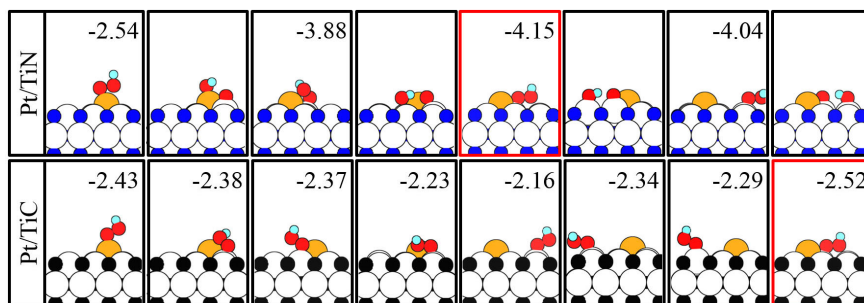The considered adsorption structures on OOH* on both Pt/TiN(100) and Pt/TiC(100), as

FIG. 2. (Color online) Side views of optimized atomic structures of the OOH* intermediate on various adsorption sites on the Pt/TiN(100) (upper panel) and Pt/TiC(100) surfaces (lower panel). The calculated adsorption energy, E_{ad} for each stable (i.e. molecularly intact) OOH* intermediate is shown (in eV) while those that undergo dissociative adsorption is not shown. The most stable adsorption configurations for Pt/TiC(100) and Pt/TiN(100) are boxed in red. The labelling of atoms here follows that in Figure 1.

well as their corresponding adsorption energies, E_{ad} (only for molecular adsorption) are shown in Figure 2.

In the lower panel of Figure 2, we find that OOH* spontaneously dissociates to O and OH upon geometry optimization for Pt/TiN(100) for most Ti-Ti and Ti-Pt bridge sites. OOH* is found to be molecularly intact on Pt/TiN(100) only when adsorbed on the Ti or Pt top sites. On the contrary, for Pt/TiC(100) (in the upper panel of Figure 2), the OOH* molecular fragment remains molecularly intact for all adsorption sites considered, with a fairly similar E_{ad} of ~ -2 eV, which may suggest that Pt/TiC(100) could potentially be a more selective catalyst system for the ORR via the series (2-electron) pathway than the Pt/TiN(100) system.

One might argue that the formation and thus the stability of OOH* could be inferred from understanding the chemistry of the O-O bond in OOH*. It was reported that the addition of H to O_2 to form OOH* weakens and elongates the O-O bond [55]. Thus, it will be informative to study the correlation between the bond distances and the adsorption chemistry of both the gas-phase and chemisorbed (most stable) OOH* and O_2 species, which are both relevant to this work. The O-O, Ti-O, and O-H bond distances have been calculated and listed in Table I, with the corresponding E_{ad} of the adsorbed species shown for comparison.

Here, we find that the adsorbed O_2 on both Pt/TiN(100) and Pt/TiC(100) are activated, i.e. having longer bond distances (1.42 and 1.47 Å, respectively) when compared to that of the gas-phase molecule (1.23 Å). The slightly longer O-O bond distance found for the Pt/TiC(100) case could be due to electron donation from the electron-rich Pt atom to O_2, which is not available for the Pt/TiN(100) case.

The evidence for this electron donation can be deduced from Figure 6 which will be discussed

TABLE I. Atomic distances for the O-O, Ti-O, and O-H atom-pairs in O_2 and OOH^*, both in the gas-phase as well as for the most stable configuration in Pt/TiN(100) and Pt/TiC(100). The accompanying adsorption energy, E^{ad} is also shown. $B_{Ti}1$, $B_{Ti}3$ and $T_{Ti}3$ denotes for the most stable Ti-Ti bridge site, the most-far Ti-Ti bridge site, and the Ti top site, respectively (See Figure 1).

System	Site	d_{O-O} (Å)	d_{Ti-O} (Å)	d_{O-H} (Å)	E^{ad} (eV)
O_2 (gas)		1.23			
OOH (gas)		1.34			
O_2 on Pt/TiN	$B_{Ti}3$	1.42	1.94		-2.59
O_2 on Pt/TiC	$B_{Ti}1$	1.47	2.09		-0.96
OOH on Pt/TiN	$T_{Ti}3$	1.43	1.98	0.97	-4.15
OOH on Pt/TiC	$B_{Ti}3$	1.49	2.00	0.97	-2.52

later. When looking at Figure 6 from Step 1 to Step 2, a change in the Bader charges of Pt is noted for O_2 adsorption. During this process, Pt in Pt/TiN(100) system gains $0.35\,e$ (Figures 6a and 6b) while Pt in Pt/TiC(100) loses $0.31\,e$ (Figures 6c and 6d). This could also explain why the Ti-O bond distance is just slightly larger for the case of Pt/TiC(100) where the actual distance from Pt may play a role.

For OOH^*, in agreement with the reported O-O bond elongation, our calculated O-O bond distance for the gas-phase OOH^* molecule is $1.34\,Å$ and this stretches even further when adsorbed on both Pt/TiN(100) and Pt/TiC(100). This is especially so for Pt/TiN(100) where the O-O bond in the OOH^* complex is almost stretched by $\sim 10\,\%$ when compared to that of its gas-phase molecule. The O-H bond distances in both systems are found to be the same.

Thus, from this comparison, we deduce that the OOH^* may be more easily activated on Pt/TiN(100) than on Pt/TiC(100), and therefore spontaneously dissociates to O and OH via the bridge sites on Pt/TiN(100).

In a nutshell, we find that the ORR intermediate molecular species of O, O_2, OH, and OOH^* prefer to adsorb further away from the embedded Pt atom in the case of Pt/TiN(100), while for the case of Pt/TiC(100), they may preferentially bind closer to the embeded Pt atom (e.g. in the case of O). This preference in adsorption is likely a result of a difference in the electron metal-support interaction (EMSI) [56] between Pt and TiN (or TiC) which may also explain their difference in the activation of oxygenated species like O_2 and OOH. Generally, we also observe that the calculated adsorption energies for the Pt/TiC(100) system are considerably weaker than that of the Pt/TiN(100) system, and we argue that these differences in adsorption geometries and
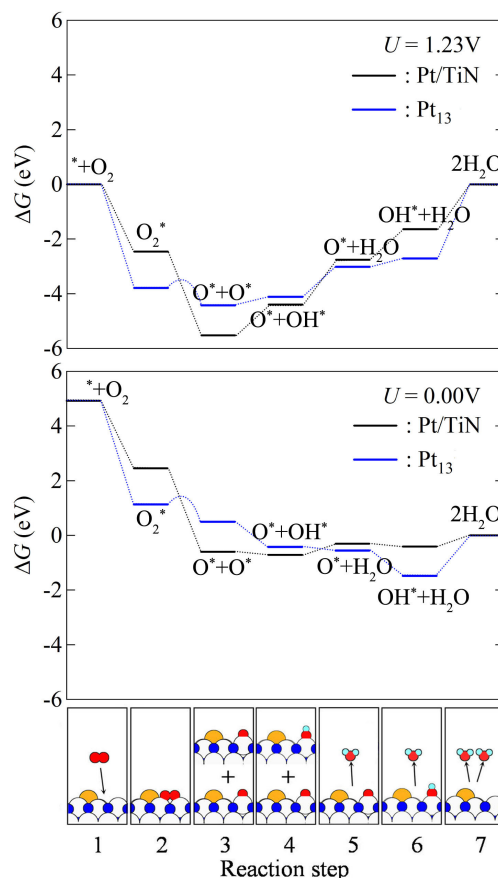
FIG. 3. (Color online) Free energy ΔG profile for the direct (4-electron) ORR pathway on Pt/TiN(100) (in black, this work) as well as the Pt_{13} cluster on graphene (in blue) which is taken from study of Lim and Wilcox [35]. The upper panel shows the ΔG profile under an external bias of 1.23 V while the middle panel shows that with zero bias [25]. Schematic cartoons of the individual steps are shown in the bottom-most panel where the labeling of atoms here follows that in Figure 1.

energies can lead to a difference in the elementary steps in the ORR on these platinized supports (which will be explained below).

B. Elementary steps of ORR on platinized supports

Turning to a closer look at the elementary reaction steps in the ORR on Pt-based systems, we choose to compare our calculated results with reported trends and values found in the literature. Using the ZPE-corrected adsorption energies above, we calculate and present the change in the free energy, ΔG (Equation 13) for direct (4-electron) ORR pathway (Steps 1 to 7, cf. Equations 4 to 9) on both Pt/TiN(100) (as denoted by the black lines) as well as the Pt_{13} cluster (as denoted by the blue lines) in Figure 3. Values for the Pt_{13} cluster are taken from former study of Lim and

Wilcox [35], and results for ΔG under an applied electropotential bias of $1.23\,\text{V}$ is also included for comparison (with the $0\,\text{V}$ case, which is similar to a reaction occurring in the gas phase). In passing, we note that atomic structures considered here are the same as in our previous work [25].

From Figure 3, without a bias voltage applied ($\sim 0\,\text{V}$), we notice the ΔG for the ORR on Pt/TiN(100) shows a strongly exothermic downhill trend in energy change and almost levels off to $\Delta G \sim 0$ after Step 3. A similar energy profile is observed for the case of the Pt_{13} cluster, with the only exception in last step where the OH undergoes a protonation, accompanied by the desorption of H_2O (Equation 9). Interestingly, from Step 2 to 3 (Equation 5), we find that dioxygen dissociation to be spontaneous (i.e. without an activation barrier) for the Pt/TiN(100) system (which is in agreement with earlier studies [54, 57]) whereas an energy barrier of $0.37\,\text{eV}$ is required for the case of the Pt_{13} cluster.

In the case where a bias voltage of $1.23\,\text{V}$ is applied, most reaction steps (after Step 3) for both Pt/TiN(100) and the Pt_{13} cluster are now energetically uphill. The largest energy uphill is found to be 1.64 and $2.71\,\text{eV}$ for Pt/TiN(100) and the Pt_{13} cluster, respectively, involving the final protonation of OH and the desorption of H_2O (Equation 9). Comparing both the supported single-atom Pt and the Pt_{13} cluster, a fairly similar ΔG profile is calculated, with the supported Pt atom exhibiting less uphill steps.

Recalling from lower panel of Figure 2, we find that the key ORR intermediate – the OOH^* molecular fragment – spontaneously dissociates to O and OH on Pt/TiN(100) for most bridge sites. This leads us to speculate that the ORR may possibly proceed via either the series (2-electron) or direct (4-electron) pathway (i.e. perhaps less selective) on Pt/TiN(100). Statistically, this very much depends on the adsorption site of the OOH intermediate during the reaction.

In Figure 4, using our calculated ZPE-corrected adsorption energies, we plot the ΔG profile for the various ORR elementary steps for both the series (2-electron) (cf. Equations 4 to 9; denoted by the blue lines) and direct (4-electron) (cf. Equations 10 and 11; denoted by the black lines) pathways for Pt/TiN(100) under zero and $1.23\,\text{V}$ bias potential.

Considering both pathways under zero bias conditions (shown in the middle panel of Figure 4), we find that both the series (2-electron) and direct (4-electron) pathways are generally downhill in energy profile. On the other hand, under an applied bias voltage of $1.23\,\text{V}$ (shown in the upper panel of Figure 4), the energy profile goes uphill after reaction Step 3, displaying very similar behaviour to the previously reported case for the Pt_{13} cluster [35].

The main difference in the energy profiles in Figure 4 comes from the different intermediates for the two different ORR pathways – O_2 dissociation for the direct (4-electron) pathway (Equa-
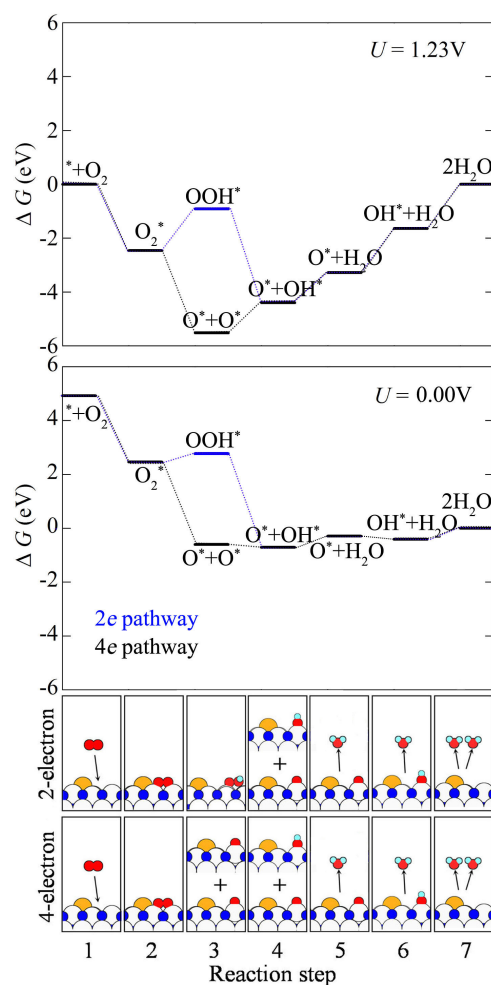
FIG. 4. (Color online) Free energy ΔG profile for the direct (4-electron, in black) and series (2-electron, in blue) ORR pathway on Pt/TiN(100) under an external potential bias of 1.23 V (shown in the upper panel), and without any bias potential (in the middle panel) [25]. Schematic cartoons of the individual steps are shown in the bottom panels where the labeling of atoms here follows that in Figure 1.

tion 5) and the stabilization of the OOH* molecular fragment for the series (2-electron) pathway (Equation 10). Here, under zero bias, a rather small energy uphill of 0.32 eV is observed for the series (2-electron) pathway (between Steps 2 and 3, cf. Equation 10) which may not be enough to discriminate the preference for either ORR pathway under technical catalysis conditions. However, under an applied bias of 1.23 V, this energy uphill is increased to a much higher value of 1.54 eV, which can be challenging to overcome thermally. Thus, it can be suggested that under an applied bias voltage, the direct (4-electron) pathway on Pt/TiN(100) may be preferred (while minimizing the uphill ΔG profile after Step 3).

In short, for the Pt/TiN(100) system, we may find no strong preference for either ORR pathways unless a "high enough" bias voltage is applied where the direct (4-electron) ORR pathway will be
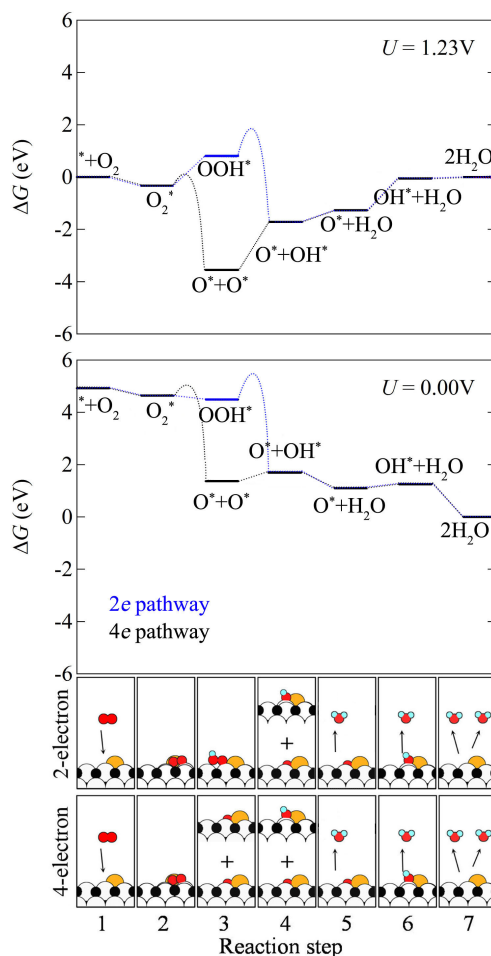
FIG. 5. (Color online) Free energy ΔG profile for the direct (4-electron, in black) and series (2-electron, in blue) ORR pathway on Pt/TiC(100) under an external potential bias of 1.23 V (shown in the upper panel), and without any bias potential (in the middle panel) [25]. Schematic cartoons of the individual steps are shown in the bottom panels where the labeling of atoms here follows that in Figure 1.

thermodynamically favoured.

Now, moving on to the other platinized system – Pt/TiC(100), we find this system to be more selective, i.e. a predominant preference for the series (2-electron) ORR pathway. From our ZPE-corrected adsorption energies of various intermediates on Pt/TiC(100), we have calculated and plotted the ΔG profile for both ORR pathways on Pt/TiC(100) in the similar fashion to that on Pt/TiN(100) (as reported above) in Figure 5.

In Figure 5, the reaction pathways with biased voltage of 0.00 and 1.23 V represent a gas-phase reaction and an electrochemical reaction, respectively. In the electrochemical reaction ($U = 1.23$ V, the upper panel of Figure 5), the highest energy uphill that determines overpotential of the catalyst system is the OOH* formation step (Step 2 to 3, cf. Equation 10) for the series (2-electron) pathway (1.01 eV) and the first oxygen protonation step (Step 3 to 4, cf. Equation 6) for the direct (4-

electron) pathway (1.64 eV). Although the activation energy for the OOH* dissociation in the series (2-electron) pathway is greater than that of the O$_2^*$ dissociation in the direct (4-electron) pathway, the energy barrier of the first protonation step (Step 3 to 4, cf. Equation 6) of the direct (4-electron) pathway is much greater than the activation energy and the highest energy uphill of the direct (2-electron) pathway. This indicates that the series (2-electron) pathway is more favored than direct (4-electron) pathway in the electrochemical reaction on Pt/TiC(100).

Considering under zero bias conditions (as shown in middle panel of Figure 5), both ORR pathways on Pt/TiC(100) show a general exothermic downhill ΔG profile. However, in the case of the more unlikely direct (4-electron) pathway (in black), the oxygen dissociation process (Step 2 to 3, cf. Equation 5) involves a rather small activation energy barrier of 0.19 eV, followed by two more small uphill processes (for Step 3 to 4, and Step 5 to 6, of 0.43 and 0.41 eV, respectively). In this aspect, the series (2-electron) ORR pathway (in blue) on Pt/TiC(100) under zero bias experiences much less uphill steps – i.e. only when the protonation of the oxygen on Pt/TiC(100), and thus we suggest the 2-electron series pathway to be favoured on Pt/TiC(100) under zero bias conditions. Here, the dissociation of the OOH* complex is also activated by 0.51 eV.

Incidentally, we would also like to highlight that the O$_2$ and OOH* activation/dissociation processes on both Pt/TiN(100) and Pt/TiC(100) are also very different. Namely, the platinized Pt/TiN(100) system presents a "barrier-less" dissociation while an activation energy barrier of 0.19 and 0.51 eV (for O$_2$ and OOH* dissociation, respectively) have been found for Pt/TiC(100). In Figure S6 of the Supplemental Material, OOH* dissociation at the Pt-topsite for both Pt/TiN and Pt/TiC systems is calculated for a more direct comparison at the same reaction site. Likewise, we find that Pt/TiN(100) also clearly shows a non-activated process of dissociating the OOH* surface complex, while a reaction energy barrier of 0.36 eV is found for Pt/TiC(100). This lends a strong support for the OOH* dissociation processes presented in Figures 4 and 5, where OOH* dissociation is indeed much more likely on Pt/TiN than on Pt/TiC.

C. Electronic structure analysis of ORR pathways on platinized supports

The higher activation barrier in Pt/TiC (rather than in Pt/TiN) may be rationally understood by examining its surface electronic structure. Via the the d-band center theory, one may correlate a stronger surface adsorption to the higher position of the d-band center (or closer in energy to the Fermi-level of the system) [23]. The projected electronic density-of-states for both Pt/TiN(100) and Pt/TiC(100) are calculated (see Figure S7 of the Supplemental Material) and the d-band centers
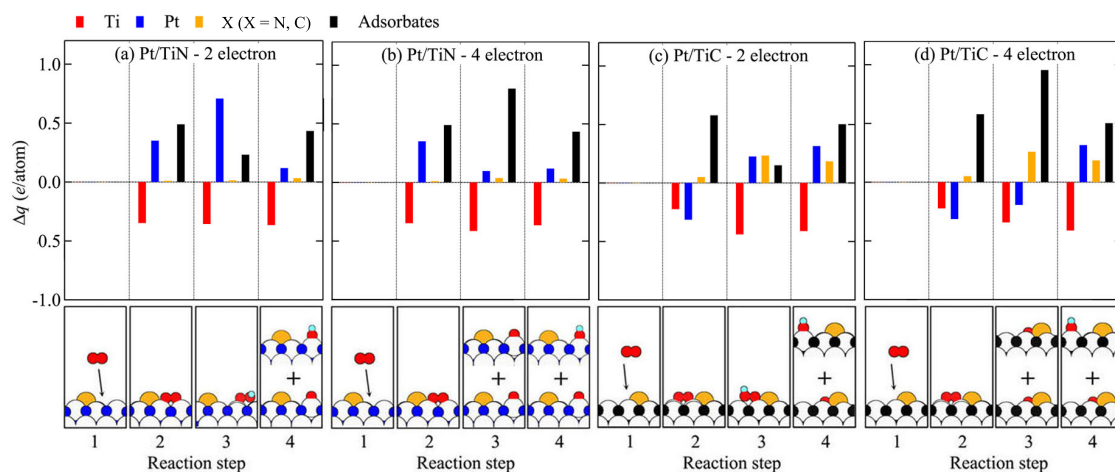
FIG. 6. (Color online) Changes in the Bader charges Δq (in e/atom) are plotted for (a) the series (2-electron) and (b) the direct (4-electron) ORR pathways on Pt/TiN(100). Likewise, that for the series (2-electron) and direct (4-electron) ORR pathways on Pt/TiC(100) are shown in (c) and (d). The labelling of atoms here follows that in Figure 1. More positive values of Δq will reflect a more negatively charged atom.

for the single-atom Pt in both Pt/TiN(100) and Pt/TiC(100) are determined to be -2.70 and $-2.75\,\text{eV}$, respectively. Although the difference is marginal, the preference for the OOH* to be relatively more strongly bound to Pt/TiN(100) than to Pt/TiC(100), rendering the dissociation process to be more activated on Pt/TiN(100). Additionally, the Pt $5d$ density-of-states of clean Pt/TiN(100) near the Fermi level is higher than that of clean Pt/TiC(100) (Figure S7), which may be attributed to the stronger OOH* adsorption on Pt/TiN(100) as discussed by Hyman and Medlin [58], where it was suggested that the strength of adsorption is highly correlated to the electron density located at or near the Fermi level.

Yet, another clue to this preference may be found from examining the changes in the surface charge states for both Pt/TiN(100) and Pt/TiC(100). We define the explicit (excess) charges for both systems via the Bader charge partitioning scheme, Δq (in e/atom) by taking the (averaged) differences of the calculated Bader charges for the selected atom in the specific system (i.e. adsorbates + support) and that in the clean Pt/TiX(100) (where X = N, C) surface or molecular reference state (i.e. Pt, Ti, N and C from Pt from Pt/TiX(100) (where X = N, C) surface, average of Ti charge state of clean Pt/TiX(100) (X = N, C) surface, average of N or C charge state of clean Pt/TiX(100) (where X = N, C) surface and the various gas-phase molecular species, respectively). For each case, a positive value will reflect a gain in electronic charges and the reverse applies.

Specifically, Δq (in e/atom) for the Pt atom, the Ti atom (i.e. closest to the adsorbed molecules), and the adsorbed molecules in each case have been calculated and plotted for the preceding series (2-electron) and direct (4-electron) ORR steps (i.e. Steps 1 to 4) in Figure 6. The reported values

for N (or C) are taken as an average of the 4 closest N (or C) atoms to chosen Ti atom at the outermost surface layer. Δq for the full pathway (i.e. Steps 1 to 7) can be found in the Supplemental Material (Figure S8). From Figure 6, we notice a clear difference in the variation of Δq values for the Pt/TiN(100) and Pt/TiC(100) systems. In Step 1, though the value is set as 0, since here we are dealing with Δq value, we determine the single-atom Pt in Pt/TiN(100) gains an overall excess charge of $0.43\,e$ while a smaller value of $0.13\,e$ is found for that in Pt/TiC(100).

For Pt/TiN(100) (as shown in Figures 6a and 6b), Δq of Pt shows comparably high value from 0.12 to $0.71\,e$ for both pathways. On the other hand, for Pt/TiC(100) (as shown in Figures 6c and 6d), Δq of Pt is found to be substantially smaller, and surprisingly even slightly negative in value (i.e. slightly more oxidized than clean Pt/TiC(100)) in Step 3. Corroborating with our calculated d-band centers, the electron density at the Fermi level, and ΔG profiles, the more negatively charged Pt in Pt/TiN(100) does indeed facilitate the dissociation of the oxygenated species in the ORR as compared to that in Pt/TiC(100).

Interestingly, we find that the Δq of N remains close to zero (i.e. almost no change from Pt/TiN(100) system) while that of C increases gradually along the reaction pathways approaching its initial bulk-like values. This seems to suggest that the former may play a minimal role electronically in assisting the ORR catalysis. More importantly, comparing the overall Δq profiles of Ti and N (or Ti and C) for both the series and direct ORR pathways, they behave fairly similarly and follow almost an identical trend (see Figure S9 of the Supplemental Material). This correlation is, however, not found for the Δq profile of the single-atom Pt, indicating that the net charge transfer between the molecular species and the supported catalyst is indeed dominated by the explicit electronic structure of the single-atom Pt catalyst.

This is inline with our previous theoretical [10, 27] and experimental [24] reports where a reduced state of Pt was reported and a more strongly reduced state indeed promotes the electrochemical ORR at a low applied bias voltage [24]. In this work, through our electronic structure analysis, we clearly demonstrate the electronic origin of the synergistic co-operative effect of the support on the electronic structure of the single-atom Pt for ORR.

Now, collectively, from our calculated DFT ΔG energy profiles for both series (2-electron) and direct (4-electron) ORR pathways on the platinized supports, we deduce that the optimal operating applied overpotential should be rather close to $0\,V$ to favour the reaction thermodynamics. We also anticipate that while Pt/TiN(100) shows no strong preference for either ORR pathways (unless a fairly high bias voltage is applied to favour the direct (4-electron) ORR pathway), Pt/TiC(100) tends to promote the series (2-electron) ORR pathway through the stable molecular adsorption of

the OOH* intermediate.

IV. CONCLUSIONS

In this work, we have performed detailed DFT studies of the ORR pathways on both single-atom Pt/TiN(100) and Pt/TiC(100) surfaces. We find that the ORR intermediates prefer binding sites away from the Pt atom in the case of Pt/TiN(100), while for the case of Pt/TiC(100), they preferentially bind closer to the Pt atom, albeit weaker than that on Pt/TiN(100). In agreement with previous studies, the O_2 and OOH* dissociation processes on Pt/TiN(100) are non-activated (i.e. "barrier-less" dissociation) while that on Pt/TiC(100) involve an activation barrier of 0.19 and 0.51 eV, correspondingly. Due to the stable molecular adsorption of OOH* on Pt/TiC(100) and the activated dissociation processes, the series (2-electron) ORR pathway (which is characterized by the stable OOH* molecular intermediate) on Pt/TiC(100) is preferred. From our electronic structure analysis, it is evident that TiN and TiC exert a strong synergistic co-operative effect on the reduced state of the single-atom Pt catalyst and is inline with recent experiments where the reduced state of Pt strongly promotes the electrochemical ORR at a low applied bias voltage.

ACKNOWLEDGMENTS

---

[1] J. H. Park, Y. Sohn, D. H. Jung, P. Kim, and J. B. Joo, "Pt deposited PtPd/C electrocatalysts with the enhanced oxygen reduction activity," J. Ind. Eng. Chem. **36**, 109–115 (2016).

[2] N. Y. Kim, J. H. Lee, J. A. Kwon, S. J. Yoo, J. H. Jang, H.-J. Kim, D.-H. Lim, and J. Y. Kim, "Vanadium nitride nanofiber membrane as a highly stable support for Pt-catalyzed oxygen reduction reaction," J. Ind. Eng. Chem. **46**, 298–303 (2017).

[3] D.-H. Kim, D.-H. Kwak, S.-B. Han, M.-C. Kim, H.-S. Park, J.-Y. Park, J.-E. Won, K.-B. Ma, and K.-W. Park, "Electrochemical catalytic contribution of transition metals at the center of porphyrin macrocycle structures as catalysts for oxygen reduction reaction," J. Ind. Eng. Chem. **54**, 200–204 (2017).

[4] J. Zhang, *PEM Fuel Cell Electrocatalysts and Catalyst Layers* (Springer, 2008).

[5] M. K. Debe, "Electrocatalyst Approaches and Challenges for Automotive Fuel Cells," Nature **486**, 43–51 (2012).

[6] A. Rabis, P. Rodriguez, and T. J. Schmidt, "Electrocatalysis for Polymer Electrolyte Fuel Cells: Recent Achievements and Future Challenges," ACS Catal. **2**, 864–890 (2012).

[7] J. Greeley, I. E. L. Stephens, A. S. Bondarenko, N. P. Johansson, H. A. Hansen, T. F. Jaramillo, J. Rossmeisl, I. Chorkendoff, and J. K. Nørskov, "Alloys of Platinum and Early Transition Metals as oxygen Reduction Electrocatalysts," Nat. Chem. **1**, 552–556 (2009).

[8] V. Stamenkovic, B. S. Mun, K. J. J. Mayrhofer, P. N. Ross, N. M. Markovic, J. Rossmeisl, J. Greeley, and J. K. Nørskov, "Changing the Activity of Electrocatalysts for Oxygen Reduction by Tuning the Surface Electronic Structure," Angew. Chem. Int. Ed. **45**, 2897–2967 (2006).

[9] D. S. Kim, C. Kim, J. K. Kim, J. H. Kim, H. H. Chun, H. Lee, and Y. T. Kim, "Enhanced Electrocatalytic Performance due to Anomalous Compressive Strain and Superior Electron Retention Properties of Highly Porous Pt Nanoparticles," J. Catal. **69**, 69–78 (2012).

[10] Y. J. Tak, W. Jang, N. A. Richter, and A. Soon, "A rational computational study of surface defect-mediated stabilization of low-dimensional Pt nanostructures on TiN(100)," Phys. Chem. Chem. Phys. **17**, 9680–9686 (2015).

[11] B. Qiao, A. Wang, X. Yang, L. F. Allard, Z. Jiang, Y. Cui, J. Liu, J. Li, and T. Zhang, "Single-Atom Catalysis of CO Oxidation Using Pt_1/FeO_x," Nat. Chem. **3**, 634–641 (2011).

[12] H. Wei, X. Liu, A. Wang, L. Zhang, B. Qiao, X. Yang, Y. Huang, S. Miao, J. Liu, and T. Zhang, "FeO_x-supported Platinum Single-atom and Pseudo-single-atom Catalysts for Chemoselective Hydrogenation of Functionalized Nitroarenes," Nat. Commun. **5**, 5634 (2014).

[13] J. D. Kistler, N. Chotigkrai, P. Xu, B. Enderle, P. Praserthdam, C. Chen, N. D. Browning, and B. C. A. Gates, "A Single-Site Platinum CO Oxidation Catalyst in Zeolite KLTL: Microscopic and Spectroscopic Determination of the Locations of the Platinum Atoms," Angew. Chem. Int. Ed. **53**, 9050–9053 (2014).

[14] J. H. Kwak, J. Z. Hu, D. Mei, C. W. Yi, D. H. Kim, C. H. F. Peden, L. F. Allard, and J. Szanyi, "Coordinatively Unsaturated Al^{3+} Centers as Binding Sites for Active Catalyst Phases of Platinum on gamma-Al_2O_3," Science **325**, 1670–1673 (2009).

[15] M. Moses-DeBusk, M. Yoon, L. F. Allard, D. R. Mullins, Z. Wu, X. Yang, G. Veith, G. M. Stocks, and C. K. Narula, "CO Oxidation on Supported Single Pt Atoms: Experimental and Ab initio Density Functional Studies of CO Interaction with Pt Atom on θ-Al_2O_3(010) Surface," J. Am. Chem. Soc. **135**, 12634–12645 (2013).

[16] J. Deng, H. B. Li, J. P. Xiao, Y. C. Tu, D. H. Deng, H. X. Yang, H. F. Tian, J. Q. Li, P. J. Ren, and X. H. Bao, "Triggering the Electrocatalytic Hydrogen Evolution Activity of the Inert Two-dimensional MoS_2 Surface via Single-atom Metal Doping," Energ. Environ. Sci. **8**, 1594–1601 (2015).

[17] Y. H. Li, J. Xing, X. H. Yang, and H. G. Yang, "Cluster Size Effects of Platinum Oxide as Active Sites in Hydrogen Evolution Reactions," Chem. Eur. J. **20**, 12377–12380 (2014).

[18] A. Boltasseva and V. M. Shalaev, "All That Glitters Need Not to Be Gold," Science **347**, 1308–1310 (2015).

[19] Y. Shao, G. Yin, and Y. Gao, "Understanding and Approaches for the Durability Issues of Pt-Based Catalysts for PEM Fuel Cell," J. Power Sources **171**, 558–566 (2007).

[20] B. Avasarala, T. Murray, W. Li, and P. Haldar, "Titanium Nitride Nanoparticles Based Electrocatalysts for Proton Exchange Membrane Fuel Cells," J. Mater. Chem. **19**, 1803–1805 (2009).

[21] B. Avasarala and P. Haldar, "Electrochemical Oxidation Behavior of Titanium Nitride Based Electrocatalysts Under PEM Fuel Cell Conditions," Electrochim. Acta **55**, 9024–9034 (2010).

[22] K. Kakinuma, Y. Wakasagi, M. Uchida, T. Kamino, H. Uchida, S. Deki, and M. Watanabe, "Preparation of Titanium Nitride-Supported Platinum Catalysts With Well Controlled Morphology and Their Properties Relevant to Polymer Electrolyte Fuel Cells," Electrochim. Acta. **77**, 279–284 (2012).

[23] S. Yang, D. Y. Chung, Y. J. Tak, J. Kim, H. Han, J. Yu, A. Soon, Y. Sung, and H. Lee, "Electronic Structure Modification of Platinum on Titanium Nitride Resulting in Enhanced Catalytic Activity and Durability for Oxygen Reduction and Formic Acid Oxidation," Appl. Catal. B **174**, 35–42 (2015).

[24] S. Yang, J. Kim, Y. J. Tak, A. Soon, and H. Lee, "Single-atom Catalyst of Platinum Supported on Titanium Nitride for Selective Electrochemical Reactions," Angew. Chem. Int. Ed. **55**, 2058–2062 (2016).

[25] S. Yang, Y. J. Tak, J. Kim, A. Soon, and H. Lee, "Support Effect in Single-atom Platinum Catalyst for Electrochemical Oxygen Reduction," ACS Catal. **7**, 1301–1307 (2017).

[26] J. A. Kwon, M.-S. Kim, D. Y. Shin, J. Y. Kim, and D.-H. Lim, "First-principles understanding of durable titanium nitride (TiN) electrocatalyst supports," J. Ind. Eng. Chem. **49**, 69–75 (2017).

[27] R. Q. Zhang, T. H. Lee, B. D. Yu, C. Stampfl, and A. Soon, "The Role of Titanium Nitride Supports for Single-Atom Platinum-Based Catalysts in Fuel Cell Technology," Phys. Chem. Chem. Phys. **14**, 16552–16557 (2012).

[28] R. Q. Zhang, C. E. Kim, B. D. Yu, C. Stampfl, and A. Soon, "Mitigation of CO Poisoning on Functionalized PtTiN Surfaces," Phys. Chem. Chem. Phys. **15**, 19450–19456 (2013).

[29] J. K. Nøskov, J. Rossmeisl, A. Logadottir, L. Lindqvist, J. Kitchin, T. Bligaard, and J. Jónsson, "Origin of the Overpotential for Oxygen Reduction at a Fuel-Cell Cathode," J. Phys. Chem. B **108**, 17886–17892 (2004).

[30] A. Ignaszak, C. Song, W. Zhu, A. Bauer, R. Baker, V. Neburchilov, S. Ye, and S. Campbell, "Titanium Carbide and its Core-shelled Derivative TiC@TiO$_2$ as Catalyst Supports for Proton Exchange Membrane Fuel Cells," Electrochim. Acta **69**, 397–405 (2012).

[31] Z. Jin, P. Li, and D. Xiao, "Enhanced Electrocatalytic Performance for Oxygen Reduction via Active Interfaces of Layer-By-Layered Titanium Nitride/Titanium Carbonitride Structures," Sci. Rep. **4**, 6712 (2014).

[32] M. Roca-Ayats, G. García, M. A. Peña, and M. V. Martínez-Huerta, "Titanium Carbide and Carbonitride Electrocatalyst Supports: Modifying PtTi Interface Properties by Electrochemical Potential Cycling," J. Mater. Chem. A **2**, 18786–18790 (2014).

[33] Z. Qiu, H. Huang, J. Du, X. Tao, Y. Xia, T. Feng, Y. Gan, and W. Zhang, "Biotemplated Synthesis of Bark-Structured TiC Nanowires as Pt Catalyst Supports With Enhanced Electrocatalytic Activity and Durability for Methanol Oxidation," J. Mater. Chem. A **2**, 8003–8008 (2014).

[34] V. Tripković, E. Skúlason, S. Siahrostami, J. K. Nørskov, and J. Rossmeisl, "The Oxygen Reduction Reaction Mechanism on Pt(111) From Density Functional Theory Calculations," Electrochim. Acta **55**, 7975–7981 (2010).

[35] D.-H. Lim and J. Wilcox, "Mechanisms of the Oxygen Reduction Reaction on Defective Graphene-Supported Pt Nanoparticles from First-Principles," J. Phys. Chem. C **116**, 3653–3660 (2012).

[36] M. Nguyen, N. Seriani, S. Piccinin, and R. Gebauer, "Photo-Driven Oxidation of Water on α-Fe_2O_3 Surfaces: An *Ab Initio* Study," J. Chem. Phys. **140**, 064703 (2014).

[37] E. Yeager, "Electrocatalysts for O_2 Reduction," Electrochim. Acta **29**, 1527–1537 (1984).

[38] M. Marković, J. Schmidt, V. Stamenković, and N. Ross, "Oxygen Reduction Reaction on Pt and Pt Bimetallic Surfaces: A Selective Review," Fuel Cells **1**, 105–116 (2001).

[39] B. Ballbuena J. Lamas, "Oxygen Reduction on $Pd_{0.75}Co_{0.25}$(111) and $Pt_{0.75}Co_{0.25}$(111) Surfaces: an *Ab Initio* Comparative Study," J. Chem. Theory. Comput. **2**, 1388–1394 (2006).

[40] R. Adzic, *Electrocatalysis* (Wiley-VCH: New York, 1998).

[41] J. P. Perdew, K. Burke, and M. Ernzerhof, "Generalized Gradient Approximation Made Simple," Phys. Rev. Lett. **77**, 3865–3868 (1996).

[42] G. Kresse and J. Hafner, "*Ab Initio* Molecular Dynamics for Liquid Metals," Phys. Rev. B **47**, 558 (1993).

[43] G. Kresse and J. Hafner, "*Ab Initio* Molecular-Dynamics Simulation of the Liquid-MetalAmorphous-Semiconductor Transition in Germanium," Phys. Rev. B **49**, 14251 (1994).

[44] G. Kresse and J. Furthmüller, "Efficient Iterative Schemes for *Ab Initio* Total-Energy Calculations Using a Plane-Wave Basis Set," Phys. Rev. B **54**, 11169 (1996).

[45] T. H. Lee, B. Delley, C. Stampfl, and A. Soon, "Environment-Dependent Nanomorphology of TiN: The Influence of Surface Vacancies," Nanoscale **4**, 5183–5188 (2012).

[46] See Supplemental Material at [URL will be inserted by publisher] for additional computational details on Pt/TiC system, calculated binding energy and electronic structure of each reaction steps.

[47] A. A. Peterson, F. Abild-Pedersen, F. Studt, J. Rossmeisl, and J. K. Nøskov, "How Copper Catalyzes the Electroreduction of Carbon Dioxide Into Hydrocarbon Fuels," Energy Environ. Sci. **3**, 1311–1315 (2010).

[48] P. W. Atkins, *Physical Chemistry, 6th ed*, Vol. 942 (Oxford University Press, New York, 1998).

[49] G. Henkelman, B. Uberuga, and H.Jónsson, "A Climbing Image Nudged Elastic Band Method for Finding Saddle Points and Minimum Energy Paths," J. Chem. Phys. **113**, 9901–9904 (2000).

[50] G. S. Karlberg, J. Rossmeisl, and J. K. Nørskov, "Estimations of Electric Field Effects on the Oxygen Reduction Reaction Based on the Density Functional Theory," Phys. Chem. Chem. Phys. **9**, 5158–5161 (2007).

[51] R. F. W. Bader, *Atoms in Molecules - A Quantum Theory* (Oxford University Press, New York, 1990).

[52] R. F. W. Bader, "A Quantum Theory of Molecular Structure and Its Applications," Chem. Rev. **91**, 893–928 (1991).

[53] G. Henkelman, A. Arnaldsson, and H. Jónsson, "A fast and Robust Algorithm for Bader Decomposition of Charge Density," Comp. Mat. Sci. **36**, 354–360 (2006).

[54] M. Hong, D. H. Lee, S. R. Phillpot, and S. B. Sinnott, "A Mechanism for TiO_2 Formation on Stepped TiN(001) from First-Principles Calculations," J. Phys. Chem. C **118**, 384–388 (2014).

[55] L. C. Grabow, B. Hwolbæk, H. Galsig, and J. K. Nørskov, "Search Directions for Direct H_2O_2 Synthesis Catalysts Starting from Au_{12} Nanoclusters," Top Catal. **55**, 336–344 (2012).

[56] P. Hu, Z. Huang, Z. Amghouz, M. Makkee, F. Xu, F. Kapteijn, A. Dikhtiarenko, Y. Chen, X. Gu, and X. Tang, "Electronic MetalSupport Interactions in Single-Atom Catalysts," Angew. Chem. Int. Ed. **53**, 3418–3421 (2014).

[57] J. Graciani, J. Fdez Sanz, T. Asaki, K. Nakamura, and J. A. Rodriguez, "Interaction of Oxygen With TiN (001): N↔O Exchange and Oxidation Process," J. Chem. Phys. **126**, 244713 (2007).

[58] M. P. Hyman and J. W. Medlin, "Effects of Electronic Structure Modifications on the Adsorption of Oxygen Reduction Reaction Intermediates on Model Pt(111)-Alloy Surfaces," J. Phys. Chem. C **111**, 17052–27060 (2007).